Source mechanism of a lower crust earthquake beneath the Himalayas and its possible relation to metamorphism

Celso Alvizuri and György Hetényi

Institute of Earth Sciences, University of Lausanne, Switzerland

Abstract

The nature of deep-crustal, intermediate and deep-focus earthquakes and their relation to metamorphic reactions is a topic of debate. Here we seek to better understand a possible link between the earthquake process and metamorphism by analyzing the mechanism of ongoing deep-crustal earthquakes. We focus on a region in the Himalayas with observed seismicity at depths expected to experience active eclogite-facies metamorphism and dehydration reactions. There are few permanent seismic stations in the region, therefore we use waveform data from a temporary seismic array deployment. We find two earthquakes with magnitude and station coverage adequate for moment tensor inversion. For a given earthquake we estimate its seismic full moment tensors (and magnitude) together with uncertainties using all available waveforms. For the largest earthquake (Mw 3.7) we obtain a best-fitting moment tensor and uncertainties that show a double-couple with a tensional crack component. In the context of geological records that document similar processes, and of laboratory experiments conducted at spatial scales that are 5-6 orders of magnitude smaller, this mechanism may be related to dehydration-driven stress changes triggering slight crack opening, and ambient stresses favoring slip along a fault.

Keywords: Himalaya, metamorphism, earthquake, seismic moment tensor, uncertainty estimates, dehydration embrittlement

Author's version of article published in Tectonophysics, `https://doi.org/10.1016/j.tecto.2019.06.023`

1. Introduction

The occurrence of earthquakes in the lower crust and upper mantle is well documented in earthquake catalogues and in geological observations. Their physical mechanisms, however, are not well understood as the host rock at such depths is expected to be ductile rather than brittle (e.g., Frohlich, 1989; Green & Houston, 1995; Prieto et al., 2013). Numerous observations of exhumed pseudotachylite, a type of glass that can form from frictional heating during rapid faulting, provide evidence of ancient earthquakes in the lower crust (e.g., Austrheim et al., 1997; Andersen et al., 2008; Hawemann et al., 2018). Based on petrological observations in the field (e.g., in the Norwegian Caledonides; Austrheim et al., 1994, 1997) these earthquakes have been interpreted in connection with eclogitization, a process in which rocks undergo mineralogical phase changes and up to 15% densification. This process can involve dehydration reactions, and is also proposed to occur in subducted oceanic crust, and to cause part of the globally observed intermediate-depth seismicity (e.g., Hacker et al., 2003).

The Himalaya collision zone, where the India plate underthrusts the Tibetan plateau at a rate of ca 2 cm/yr, provides a unique and modern setting for studying seismicity together with metamorphism. Receiver function studies for the region show that the India plate lower crust reaches depths of 55-80 km (Schulte-Pelkum et al., 2005; Nábělek et al., 2009; Wittlinger et al., 2009); and a combined geophysical-petrological model suggests that the crust at these depths is partially hydrated and is expected to experience active eclogitization through dehydration reactions (Hetényi et al., 2007). Earthquakes have also been detected in the same area and depth range by a temporary seismic broadband array (Monsalve et al., 2006). Furthermore, the crustal root of Tibet is the only place on Earth where deep-crustal earthquakes can be studied in the continental lithospheric context. Here we analyze the mechanisms for these earthquakes and their possible relation to metamorphic dehydration reactions.

On much smaller scales, laboratory experiments also aim to explain lower-crustal, intermediate and deep-focus earthquakes by subjecting rocks to similar temperature and pressure conditions, studying their mineralogical phase changes and analyzing their acoustic emissions. In this context, three physical mechanisms are usually considered: (1) Transformational faulting, where minor cracks, which open during metamorphic densification of the rock, evolve into shear-bands and then form a fault zone (e.g., Green et al., 1990); (2) Dehydration embrittlement, in which pore fluid pressure increases to cause mechanical failure of the rock (e.g., Green & Houston, 1995; Okazaki & Hirth, 2016; Hacker et al., 2003; Jung et al., 2004); (3) Thermal runaway, in which a shear instability develops following local heating due to viscous creep (e.g., Kelemen & Hirth, 2007; John et al., 2009; Braeck & Podladchikov, 2007).

In this study we estimate seismic moment tensors for the two largest earthquakes beneath the Himalayas, at about 70 km depth, that were recorded during a temporary seismic array deployment. In our analysis we use the earthquake waveforms to find a best-fitting focal mechanism by performing a grid search over the full space of moment tensors. We analyze the moment tensor uncertainties to discern among mechanisms such as the double-couple, cracks, and isotropic. The methodology has proven successful in source discrimination and for a range of seismic sources and settings including tectonic, volcanic, and nuclear tests (Alvizuri & Tape, 2016; Alvizuri et al., 2018; Alvizuri & Tape, 2018). We find that our moment tensor solutions show non-double-couple components. We analyze the results in terms of seismic source models, and discuss them in the context of metamorphic dehydration reactions in the lower crust.

2. Data and Method

2.1. Seismological data

2.1.1. Data collection

Our study area in the Himalayas is sparsely populated, and there are few permanent broadband seismic stations available. We therefore focus on data from two temporary seismic array deployments in the Himalayas; the HImalaya

Nepal Tibet Seismic Experiment (HIMNT) which operated 27 three-component broadband seismic stations between 2001-2003 in Eastern Nepal and South-Central Tibet (Sheehan, 2001) (Figure 1), and the Geodynamics ANd Seismic Structure of the Eastern-Himalaya Region (GANSSER) array which deployed 38 stations in 2013-2014 in Bhutan (Swiss Seismological Service (SED), 2013). The two arrays shared similar goals of studying seismicity, seismotectonics and lithospheric structure of the Himalayas.

2.1.2. Seismic event catalogs

A total of 1649 local earthquakes were detected by the HIMNT array, of which 538 were relocated (Monsalve et al., 2006) (Figure 1). From the relocated events we identified 39 events below 50 km depth with magnitudes M>1 and epicenters within the array. In order to find events suitable for moment tensor analysis we inspected the signal-to-noise-ratio in their waveforms, performed preliminary moment tensor inversions, and verified station coverage. We found that only the two largest events, with magnitudes M<4 and depths of 68 and 76 km, are suitable candidates for moment tensor analysis (Figure 1). In comparison with the moment tensor estimates by de la Torre et al. (2007), which is restricted to the deviatoric moment tensor, we search the space of full moment tensors. Within the GANSSER catalog (Diehl et al., 2017) only the 2013-06-06 earthquake at 76 km depth fit our depth criteria, but it has insufficient azimuthal coverage (gap>180°). We therefore focus our study on the main event in South Tibet near East Nepal, and present solutions for the smaller event there in the Supplementary Material.

2.1.3. Preparation of waveform data

Our main event is relatively deep, relatively small, it generated surface waves discernible primarily on the transverse component, and in some stations its body waveform amplitudes are relatively larger toward higher frequencies. For our main result we used 33 traces recorded at 13 different stations, with vertical and radial component P-waves filtered between 0.4-0.8 Hz, and transverse component surface waves filtered between 0.04-0.06 Hz.

2.1.4. Seismic structure models for the region

Our moment tensor method involves comparing observed with synthetic seismograms derived from a given wavespeed model. We consider two layered models, one for East Nepal and one for South Tibet, that were obtained using HIMNT data and joint inversion of hypocenters and wavespeed (Monsalve et al., 2006). The two models differ by less than 1 percent wavespeed at shallower depths (above 55 km), and differ primarily in their Moho which deepens from East Nepal to South Tibet by 15 km. The earthquakes in this study have hypocenters beneath South Tibet, and their raypaths towards seismic stations at the surface span this zone of transitional wavespeeds and Moho depths. Given that the South Tibet model is more representative of the hypocenter zones, and the small wavespeed differences between models at shallower depths, we chose this model in our final results. Seismic attenuation also varies from east Nepal to south Tibet, and we adapted the velocity model with attenuation values estimated with HIMNT data (Sheehan et al., 2013); this structural model is deduced from a joint inversion of hypocenters and velocities. Given the variability of local Moho depths from receiver function analyses (Schulte-Pelkum et al., 2005), we cannot rule out that the hypocenter of our main event at 76 km depth is in the uppermost mantle, but we consider this event as part of the crustal seismicity between about 60-70 km depth (Figure 1).

2.2. Full moment tensor methodology

The seismic moment tensor $\mathbf{M}$ is a 3×3 symmetric matrix that characterizes a seismic source such as an earthquake within the Earth. A moment tensor $\mathbf{M}$ can be expressed in terms of its eigenvalues $\mathbf{\Lambda} = [\lambda_1, \lambda_2, \lambda_3]$ and a rotation matrix $\mathbf{U}$ as $\mathbf{\Lambda} = \mathbf{U}[\mathbf{\Lambda}]\mathbf{U}^{-1}$. The source type of $\mathbf{M}$ is the normalized eigenvalue triple $\mathbf{\Lambda} = \hat{\mathbf{\Lambda}}/\|\hat{\mathbf{\Lambda}}\|$. The source types for all moment tensors make up the fundamental lune representation on the unit sphere (Tape & Tape, 2012). In order to compare probabilities for source types for a given event, we use an equivalent representation of the lune on a rectangle with coordinates (v, w), discussed in the next section.

Our inversion method involves performing a complete search over the full parameter space of moment tensors (lune longitude, lune latitude, strike, dip, and rake) including magnitude and depth. We use a version of the cut-and-paste code (Zhao & Helmberger, 1994; Zhu & Helmberger, 1996; Zhu & Ben-Zion, 2013) that was recently changed with a geometric parameterization for moment tensors and their uncertainty quantification (Alvizuri & Tape, 2016; Silwal & Tape, 2016; Alvizuri et al., 2018). For each moment tensor in the parameter space, synthetic seismograms are computed using a frequency-wavenumber approach (Zhu & Rivera, 2002) with a 1D (layered) Earth model, and then these seismograms are compared with observed waveforms via a misfit function. For details, see Alvizuri et al. (2018).

2.3. Decomposition into physical mechanisms

Following the discussion in Tape & Tape (2013) we consider two seismic source models for the earthquake analyzed here. In the classical model from Aki & Richards (1980) and elucidated by Dufumier & Rivera (1997), a source is described as (perhaps oblique) slip on a planar fault, with two parameters characterizing the source type being the Poisson ratio ν and the angle $\alpha = \angle(\mathbf{N}, \mathbf{S})$ between the normal vector $\mathbf{N}$ and slip vector $\mathbf{S}$. With this model we find that the Poisson ratios for the main event are not well constrained, and therefore we do not pursue this analysis further. In the crack-plus-double-couple (CDC) model which was introduced by Minson et al. (2007) a source is described as a crack tensor plus a double-couple tensor. The two parameters that characterize the CDC model are the azimuth ϕ on the lune and the crack fraction ζ which relate to the moment tensor as (Tape & Tape, 2013)

$$\mathbf{M}(\phi, \zeta) = (\cos\zeta)\mathbf{D} + (\sin\zeta)\mathbf{K}(\phi) \tag{1}$$

where $0 \leq \zeta \leq \pi/2$, $\mathbf{D}$ is a double-couple tensor, and $\mathbf{K}(\phi)$ is a crack tensor. The angle ϕ is the azimuth of crack tensors on the lune boundary (counterclockwise from top), and ζ provides a measure of double-couple ($\zeta = 0°$) versus crack ($\zeta = 90°$) tensors. We seek to gain insight into the source model by analyzing the ensemble of moment tensors evaluated in our grid search. For any given event, our algorithm computes a probability density for source types $p = p(v, w)$ which represents the probability at every source-type location. Using p we then sample the ensemble of all moment tensor solutions for a given event with the rejection method (e.g., Tarantola, 2005), and use the samples to calculate the ϕ and ζ distributions.

3. Results

3.1. Moment tensor and uncertainty analysis

We show the results for our main event in Figures 2–3 (Figure S1 summarizes the grid search for the best-fitting depth). The grid search for the best-fitting moment tensor in Figure 2 reveals a mechanism with magnitude M_{w} 3.7 at a depth of 76 km. The waveforms in Figure 2 show synthetic seismograms (red lines), computed for the best-fitting mechanism, in comparison with the observed seismograms (black lines). The amplitude difference at some stations (e.g. DINX, BUNG) could use some improvements, and considering that this event is relatively small, deep, and our knowledge of the structure at such depths is limited, as discussed in Section 2, the overall similarity between observed and synthetic shows a degree of success in our estimates.

A summary uncertainty analysis for our estimated moment tensor is shown in Figure 3, and a more detailed version which includes the best-fitting mechanisms and orientation for each source type, and a confidence parameter for source types (Tape & Tape, 2016) is shown in Figure S2. The best-fitting moment tensor is represented by the beachball in Figure 3a, a lune plot showing waveform fit (variance reduction) by source type is shown on Figure 3b, and a probability density $p(v, w)$ for source types is shown on Figure 3c. The best-fitting solution on the lune (Figure 3b) is at $(\gamma, \delta) = (-5°, 17°)$, where (γ, δ) represent the longitude (CLVD) and latitude (ISO) coordinates on the lune. The variation of waveform misfit reveals a crescent-shape region above the double-couple with similar-fitting mechanisms. The probability density $p(v, w)$ (Figure 3c) shows a similar but broader crescent shape. This result is calculated by considering all moment tensor orientations within each cell, therefore the most probable source type does not necessarily coincide with the best-fitting source type. In our case, the most probable solution lies at $(\gamma, \delta) = (22°, 26°)$.

3.2. Analysis of source models

Figure 4 provides a starting point for interpreting the physical source model for our moment tensor solution. This figure shows the probability densities for the angles ϕ and ζ in equation [1]. For comparison, the black curves show the same angles but calculated analytically for a homogeneous distribution of moment tensors (Tape & Tape, 2015). For an ideal seismic source with a simple and well-defined source type (e.g., a pure crack), the histograms for ϕ and ζ would show well defined peaks above the homogeneous distribution. Our results show a range of crack tensors between azimuths $\phi = -35°$ and $\zeta = 145°$ above the homogeneous distribution that provide similar fitting solutions, as also seen in Figure 3c. Then, in comparing the relative amounts of double-couple versus crack tensors, the population of ζ peaks at about 25° away from the double-couple. Figures 3–4 are complementary except Figure 3 also describes the spread of our solution compared to the homogeneous distribution for moment tensors.

4. Discussion

4.1. Interpretation

Our seismic source analysis for the deep Himalayan earthquake reveals a range of similar-fitting moment tensors with a tensional crack component. In the context of the India lower crust beneath southern Tibet, this mechanism may be related to metamorphic reactions, during which water is expelled from the host rock through dehydration reactions. The dehydrated water in the pores then incrementally increases the fluid pressure and reduces the normal stress.

With time, the pores connect to open a fracture, along which slip is favored by ambient differential stresses (Jung et al., 2004). This mechanism also works for relatively small amounts of fluid release, as soon as the amount of fluid exceeds the available pore volume. The initiation of the fluid escape is proposed based on field observations of dehydration veins in the Ligurian Alps (Plümper et al., 2017). Chemical heterogeneities of those rocks at the grain level cause dehydration reactions to initiate at specific sites at micrometer scales which, with varying fluid pressure, grow into vein networks across up to the meter scale (Plümper et al., 2017). This mechanism is similar to our interpretation for the India lower crust beneath southern Tibet.

Assuming a strong and dry lower continental crust, stress pulses after earthquakes in the upper crust could induce aftershocks in the lower crust and trigger metamorphic reactions (Jamtveit et al., 2018). However, based on combined thermo-kinematic and petrological model by Hetényi et al. (2007), the lower crust in our study location appears partially hydrated, and the dehydration reactions may have favored triggering the earthquake analyzed here.

4.2. Comparison to laboratory experiments

To date there is no laboratory experiment yet with partially hydrated rocks simulating the continental lower crust. Our results do not compare with the recent laboratory experiments by Shi et al. (2018) where they use dry samples and argue for shear-bands evolving into a fault zone; in fact, the choice of using dry samples in their experiments appears to be motivated by the natural samples used in Hacker et al. (2000), which are from a region in the northern part of Tibet, about 600 km farther north from our study area, and not underthrusted by the India plate.

Another recent experiment by Incel et al. (2017) uses partially hydrated (lawsonite) samples, but they note that dehydration does not play a role in triggering acoustic emissions during mineralogical reactions, as evidenced by the remaining lawsonite phase in the assemblage. Hence, the authors argue for transformational faulting induced through grain-size reduction. Moreover, dehydration in those experiments occurred at much higher temperatures (800 °C) than the expected temperature in the India lower crust (ca. 600-650 °C).

The closest laboratory conditions to our setting is that by Ferrand et al. (2017), where they use hydrated samples representative of an oceanic subduction context, and where not only dehydration embrittlement, but dehydration driven stress-transfer causes failure. Dehydration embrittlement in a subduction zone context was also demonstrated in a numerical model of coupled dehydration and deformation (Brantut et al., 2017) . Similar processes, in particular volume decrease (densification) reactions favoring triggering of dynamic shear failures, could also operate in the India lower crust.

4.3. Comparison with the geological record

The M_w 3.7 earthquake we describe would correspond to ca. 10 cm slip on a roughly few kilometers long, several ten-meters wide zone. These dimensions are comparable to natural outcrops of eclogitized rocks associated with paleo-earthquakes on Holsnøy Island (Austrheim et al., 1996). Although the water content in the rocks differs between the current Himalayan and the former Caledonian contexts, the former being partially hydrated and the latter being dry, the similar rupture sizes may be controlled by the mechanical strength of the lower crust.

4.4. Additional remarks

We cannot be sure that the primary expression of eclogitization produces the tensional crack component observed in our results. Indeed, a more logical mechanism that accommodates densification and volume decrease is a collapsing crack, or transformational faulting, as proposed by Green et al. (1990). Such processes, however, could operate on longer time scales and hence not cause earthquakes at all, or occur as smaller events. Within our focus depths beneath South Tibet, the magnitudes and depths of such events would preclude their full moment tensor analysis. On the other hand, patterns in their occurrence may reveal further insights into the process. This will be investigated in a separate study using several earthquake catalogues.

In any moment tensor analysis, as in our study, several factors may produce non-double-couple artefacts, including curved faults, and 3D structure variations, such as anisotropy and heterogeneities near the source region, that are not accounted for with a 1D layered model (e.g., Kawasaki & Tanimoto, 1981; Frohlich et al., 1989; Julian et al., 1998; Burgos et al., 2016). Future moment tensor analysis with refined 3D velocity models for the region may provide additional insight.

Finally, we cannot rule out that the earthquake at hand occurred in the uppermost mantle, even though the dehydration reactions occurred in the lower crust. The hypocenter is close to the Moho, and stress changes following the dehydration reactions may cause failure in the nearby mantle rocks instead of the lower crust, depending on their respective rheologies.

5. Conclusions

We present a full moment tensor and uncertainty analysis for a M_w 3.7 earthquake 76 km beneath Himalaya, within a region expected to experience metamorphism through eclogitization reactions. The best-fitting moment tensor is between a double-couple and a tensile crack. Its uncertainty analysis shows a localized population of low-misfit moment tensors away from the double-couple, and its source type probability density shows a broad region of solutions.

In the context of geophysical and petrological models of the India lower crust, which suggest the crust there is partially hydrated and undergoes metamorphic dehydration reactions, it is plausible that our estimated focal mechanism is related to dehydration embrittlement. This process is also observed in laboratory experiments with hydrated rocks, although with different rock compositions. This result agrees with the hypothesis that dehydration embrittlement changes the mechanical properties of the crust, and extends the depth of the brittle rupture domain to that of the deepest hydrated phases (Raleigh & Paterson, 1965;

Jung et al., 2004).

Our result focuses on a single event in the deep continental crust. Other mechanisms, such as dehydration embrittlement, transformational faulting, and thermal runaway, may apply to other contexts. The prevailing mechanism of intermediate and deep-focus earthquakes depends on the actual pressure, temperature and water-content conditions. In the India lower crust, the presence of water in the host rock is key and leads to the interpretation of a dehydration-related seismic event.

Several phenomena related to eclogitization, for example the accommodation of overall volume decrease, occur over time scales that preclude seismological analyses. Future studies, including field observations, laboratory experiments with different rock compositions and hydration levels, numerical studies of rock mechanics, as well as better constrained seismic events may further our understanding.

Acknowledgements

We thank Gaspar Monsalve for providing the HIMNT earthquake catalog, Walter Tape & Carl Tape for discussions regarding the analytic moment tensor distribution, Oliver Plümper & Neil Mancktelow for discussions on the petrological and geological aspects, and Benjamin Malvoisin, Sarah Incel, Sofia Kufner for comments that helped to improve the manuscript. We acknowledge the constructive comments by two anonymous reviewers and reviewer Kusala Rajendran. This study was funded by the Swiss National Science Foundation (grant PP00P2_157627 for project OROG3NY). The seismic data used in this study are openly available through the IRIS Data Services. The authors declare no competing financial interests.

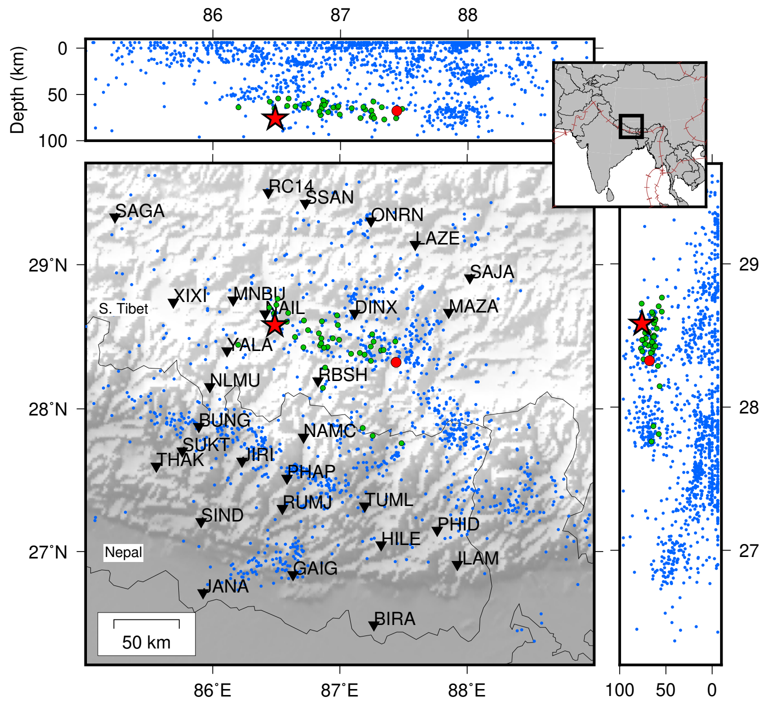

Figure 1: Hypocenters (blue circles) detected during deployment of the HIMNT seismic array (black triangles) between 2001-2003. The top and side panels show hypocenter profiles. A total of 1649 local earthquakes were located within the HIMNT array and 538 were relocated (Monsalve et al., 2006). Out of these we identified 39 events below 50 km depth with magnitudes M>1 and epicenters within the array (green circles). The largest event in this subset (red star) has magnitude Mw 3.7 and is the focus of this study. A second, smaller event (red circle) is presented in the Supplementary Material. The inset highlights E. Nepal and study area.

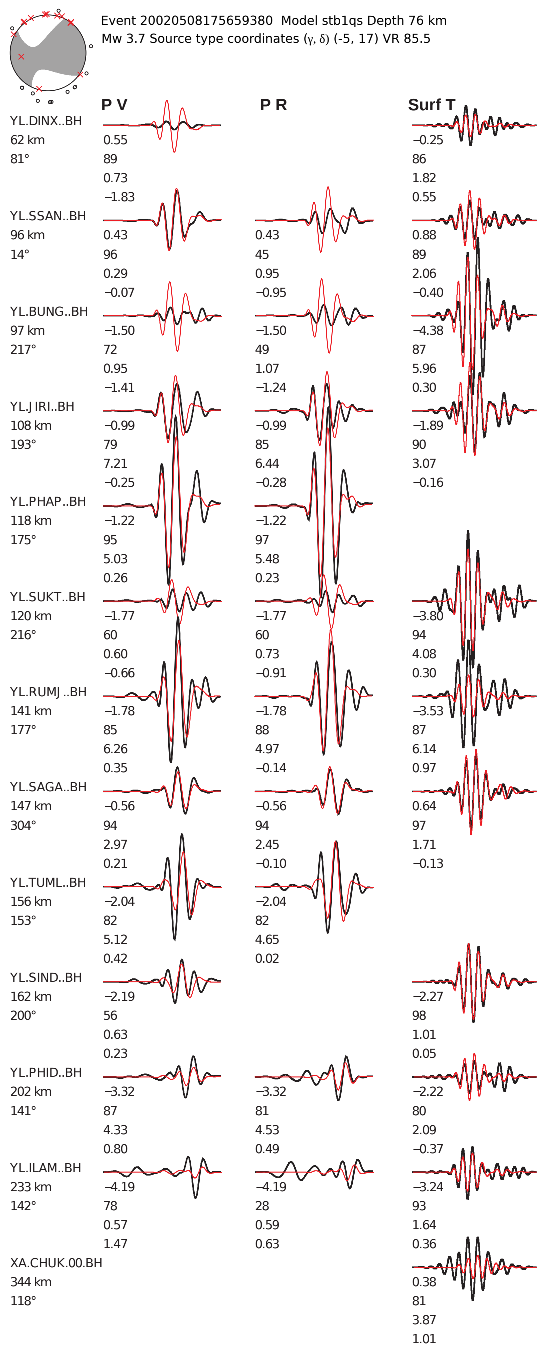

Figure 2: Moment tensor solution and waveform fits for the main event in this study. The labels include event time (2002-05-08T17:56:59 UTC), wavespeed model, estimated depth and magnitude, and source-type coordinates of the optimal solution; the beachball represents the best-fitting moment tensor and shows station distribution on the focal sphere. The observed waveforms are plotted in black, the synthetic waveforms are plotted in red. The column labels PV, PR, SurfT are for P-wave vertical, radial, and surface wave transverse components. The stations are ordered by increasing epicentral distance. Numbers beneath each station are epicentral distance and back-azimuth; numbers beneath each waveform pair are the time shift, the cross-correlation maximum, the percentage of the misfit function, and the log amplitude ratio. Waveform data from station XA.CHUK is from the Bhutan Pilot Experiment (Miller, 2002).

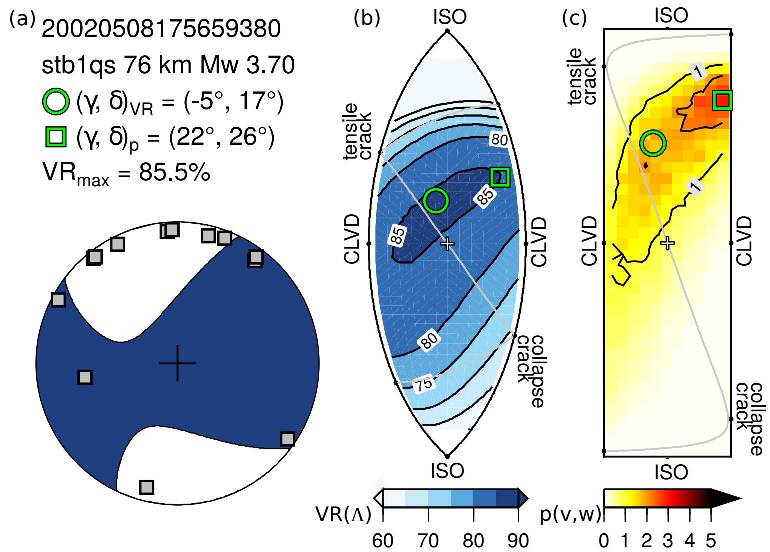

Figure 3: Moment tensor uncertainty summary for the result in Figure 2. (a) The labels include event time, wavespeed model, estimated depth and magnitude, and source-type coordinates of the optimal solution; the enlarged beachball shows station distribution on the focal sphere. (b) Waveform fit (variance reduction) plotted on the lune; regions of best-fitting solutions are darker blue. (c) Probability density function $p(v, w)$ for source types (v and w are the horizontal and vertical axes). In (b)-(c) the double-couple is represented by a cross; the gray lines separate different moment tensor regimes. The source-type coordinates for the best fitting solution in (a) are denoted by green circles, the maximum of $p(v, w)$ is denoted by green squares. See text for more details, and Figures S1-S2 for further details about moment tensors and their lune representation.

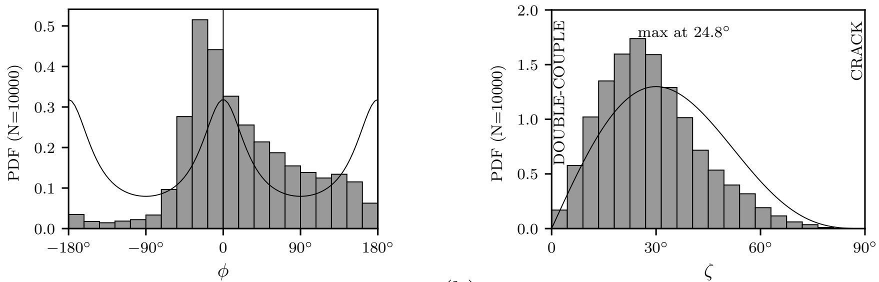

(a) (b)

Figure 4: Probability densities of the crack-plus-double-couple (CDC) source model for the main event. In the CDC model each source type is represented by (a) its azimuth ϕ on the lune (counterclockwise from top) and (b) the crack fraction ζ. For a double-couple moment tensor $\zeta = 0°$, for a tensional or compressional crack $\zeta = 90°$. The angles ϕ and ζ are calculated directly from the eigenvalues of the moment tensors, and for this result they were calculated for 10000 moment tensor samples (see Fig. S3) from the posterior distribution p(v,w) (Fig. 3c). For comparison, the black curves show the same angles but calculated analytically for a homogeneous distribution of moment tensors.

References

Aki, K., & Richards, P. G. (1980). *Quantitative Seismology, Theory and Methods*. San Francisco, Calif., USA: W. H. Freeman.

Alvizuri, C., Silwal, V., Krischer, L., & Tape, C. (2018). Estimation of full moment tensors, including uncertainties, for nuclear explosions, volcanic events, and earthquakes. *J. Geophys. Res. Solid Earth*, *123*, 5099–5119. doi:`10.1029/2017JB015325`.

Alvizuri, C., & Tape, C. (2016). Full moment tensors for small events ($M_\mathrm{w} < 3$) at Uturuncu volcano, Bolivia. *Geophys. J. Int.*, *206*, 1761–1783. doi:`10.1093/gji/ggw247`.

Alvizuri, C., & Tape, C. (2018). Full moment tensor analysis of nuclear explosions in North Korea. *Seismol. Res. Lett.*, *89*, 2139–2151. doi:`10.1785/0220180158`.

Andersen, T. B., , Mair, K., Austrheim, H., Podladchikov, Y., & Vrijmoed, J. C. (2008). Stress release in exhumed intermediate and deep earthquakes determined from ultramafic pseudotachylyte. *Geology*, *36*, 995–998. doi:`10.1130/G25230A.1`.

Austrheim, H., , & Boundy, T. M. (1994). Pseudotachylytes generated during seismic faulting and eclogitization of the deep crust. *Science*, *265*, 82–83.

Austrheim, H., Erambert, M., & Boundy, T. M. (1996). Garnets recording deep crustal earthquakes. *Earth Planet. Sci. Lett.*, *139*, 223–238.

Austrheim, H., Erambert, M., & Engvik, A. K. (1997). Processing of crust in the root of the caledonian continental collision zone: the role of eclogitization. *Tectonophysics*, *273*, 129–153.

Braeck, S., & Podladchikov, Y. Y. (2007). Spontaneous thermal runaway as an ultimate failure mechanism of materials. *Phys. Rev. Lett.*, *98*, 095504. doi:`10.1103/PhysRevLett.98.095504`.

Brantut, N., Stefanou, I., & Sulem, J. (2017). Dehydration-induced instabilities at intermediate depths in subduction zones. *J. Geophys. Res.*, *122*, 6087–6107. doi:`10.1002/2017JB014357`.

Burgos, G., Capdeville, Y., & Guillot, L. (2016). Homogenized moment tensor and the effect of near-field heterogeneities on nonisotropic radiation in nuclear explosion. *J. Geophys. Res. Solid Earth*, *121*, 4366–4389. doi:`10.1002/2015JB012744`.

de la Torre, T. L., Monsalve, G., Sheehan, A. F., Sapkota, S., & Wu, F. (2007). Earthquake processes of the Himalayan collision zone in eastern Nepal and the southern Tibetan Plateau. *Geophys. J. Int.*, *171*, 718–738. doi:`10.1111/j.1365-246X.2007.03537.x`.

Diehl, T., Singer, J., Hetényi, G., Grujic, D., Clinton, J., Giardini, D., & Kissling, E. (2017). Seismotectonics of Bhutan: Evidence for segmentation of the Eastern Himalayas and link to foreland deformation. *Earth Planet. Sci. Lett.*, *471*, 54–64. doi:10.1016/j.epsl.2017.04.038.

Dufumier, H., & Rivera, L. (1997). On the resolution of the isotropic component in moment tensor inversion. *Geophys. J. Int.*, *131*, 595–606.

Ferrand, T. P., Hilairet, N., Incel, S., Deldicque, D., Labrousse, L., Gasc, J., Renner, J., Wang, Y., Green, H. W., & Schubnel, A. (2017). Dehydration-driven stress transfer triggers intermediate-depth earthquakes. *Nature Communications*, *8*. doi:10.1038/ncomms15247.

Frohlich, C. (1989). The nature of deep-focus earthquakes. *Annu. Rev. Earth Planet. Sci.*, *17*, 227–254.

Frohlich, C., Riedesel, M. A., & Apperson, K. D. (1989). Note concerning possible mechanisms for non-double-couple earthquake sources. *Geophys. Res. Lett.*, *16*, 523–526.

Green, H. W., & Houston, H. (1995). The mechanics of deep earthquakes. *Annu. Rev. Earth Planet. Sci.*, *23*, 169–213. doi:10.1146/annurev.ea.23.050195.001125.

Green, H. W., Young, T. E., Walker, D., & Scholz, C. H. (1990). Anticrack-associated faulting at very high pressure in natural olivine. *Nature*, *348*, 720–722. doi:10.1038/348720a0.

Hacker, B. R., Abers, G. A., Peacock, S. M., & Holloway, S. D. (2003). Subduction factory 2. Are intermediate-depth earthquakes in subducting slabs linked to metamorphic dehydration reactions? *J. Geophys. Res.*, *108*. doi:10.1029/2001JB001129.

Hacker, B. R., Gnos, E., Ratschbacher, L., Grove, M., McWilliams, M., Sobolev, S. V., Wan, J., & Zhenhan, W. (2000). Hot and Dry Deep Crustal Xenoliths from Tibet. *Science*, *287*, 2463–2466. doi:10.1126/science.287.5462.2463.

Hawemann, F., Mancktelow, N. S., Wex, S., Camacho, A., & Pennacchioni, G. (2018). Pseudotachylyte as field evidence for lower-crustal earthquakes during the intracontinental petermann orogeny (musgrave block, central australia). *Solid Earth*, *9*, 629–648. doi:10.5194/se-9-629-2018.

Hetényi, G., Cattin, R., Brunet, F., Bollinger, L., Vergne, J., Nábělek, J. L., & Diament, M. (2007). Density distribution of the India plate beneath the Tibetan plateau: Geophysical and petrological constraints on the kinetics of lower-crustal eclogitization. *Earth Planet. Sci. Lett.*, *264*, 226–244.

Incel, S., Hilairet, N., Labrousse, L., John, T., Deldicque, D., Ferrand, T., Wang, Y., Renner, J., Morales, L., & Schubnel, A. (2017). Laboratory earthquakes triggered during eclogitization of lawsonite-bearing blueschist. *Earth Planet. Sci. Lett.*, *459*, 320–331. doi:10.1016/j.epsl.2016.11.047.

Jamtveit, B., Ben-Zion, Y., Renard, F., & Austrheim, H. (2018). Earthquake-induced transformation of the lower crust. *Nature*, *556*, 487–491. doi:10.1038/s41586-018-0045-y.

John, T., Medvedev, S., Rüpke, L. H., Andersen, T. B., Podladchikov, Y. Y., & Austrheim, H. (2009). Generation of intermediate-depth earthquakes by self-localizing thermal runaway. *Nature Geoscience*, *2*, 137–140. doi:10.1038/ngeo419.

Julian, B. R., Miller, A. D., & Foulger, G. R. (1998). Non-double-couple earthquakes: 1. Theory. *Rev. Geophys.*, *36*, 525–549. doi:10.1029/98RG00716.

Jung, H., Green, H. W., & Dobrzhinetskaya, L. F. (2004). Intermediate-depth earthquake faulting by dehydration embrittlement with negative volume change. *Nature*, *428*, 545–549. doi:10.1038/nature02412.

Kawasaki, I., & Tanimoto, T. (1981). Radiation patterns of body waves due to the seismic dislocation occurring in an anisotropic source medium. *Bull. Seismol. Soc. Am.*, *71*, 37–50.

Kelemen, P. B., & Hirth, G. (2007). A periodic shear-heating mechanism for intermediate-depth earthquakes in the mantle. *Nature*, *446*, 787–790. doi:10.1038/nature05717.

Miller, K. (2002). Bhutan Pilot Experiment. International Federation of Digital Seismograph Networks. Other/Seismic Network. doi:10.7914/SN/XA_2002.

Minson, S. E., Dreger, D. S., Bürgmann, R., Kanamori, H., & Larson, K. M. (2007). Seismically and geodetically determined nondouble-couple source mechanisms from the 2000 Miyakejima volcanic earthquake swarm. *J. Geophys. Res.*, *112*. doi:10.1029/2006JB004847.

Monsalve, G., Sheehan, A., Schulte-Pelkum, V., Rajaure, S., Pandey, M. R., & Wu, F. (2006). Seismicity and one-dimensional velocity structure of the Himalayan collision zone: Earthquakes in the crust and upper mantle. *J. Geophys. Res.*, *111*. doi:10.1029/2005JB004062.

Nábělek, J., Hetényi, G., Vergne, J., Sapkota, S., Kafle, B., Jiang, M., Su, H., Chen, J., & Huang, B.-S. (2009). Intermediate depth earthquakes beneath the India-Tibet Collision Zone. *Science*, *325*, 1371–1374. doi:10.1126/science.1167719.

Okazaki, K., & Hirth, G. (2016). Dehydration of lawsonite could directly trigger earthquakes in subducting oceanic crust. *Nature*, *530*, 81–84. doi:10.1038/nature16501.

Plümper, O., Timm, J., Podladchikov, Y. Y., Vrijmoed, J. C., & Scambelluri, M. (2017). Fluid escape from subduction zones controlled by channel-forming reactive porosity. *Nature Geoscience*, *10*, 150–156. doi:10.1038/ngeo2865.

Prieto, G. A., Florez, M., Barrett, S. A., Beroza, G. C., Pedraza, P., Blanco, J. F., & Poveda, E. (2013). Seismic evidence for thermal runaway during intermediate-depth earthquake rupture. *Geophys. Res. Lett.*, *40*, 6064–6068. doi:10.1002/2013GL058109.

Raleigh, C. B., & Paterson, M. S. (1965). Experimental deformation of serpentinite and its tectonic implications. *J. Geophys. Res.*, *70*, 3965–3985.

Schulte-Pelkum, V., Monsalve, G., Sheehan, A., Pandey, M. R., Sapkota, S., Bilham, R., & Wu, F. (2005). Imaging the Indian subcontinent beneath the Himalaya. *Nature*, *435*, 1222–1225. doi:10.1038/nature03678.

Sheehan, A. (2001). Himalayan Seismotectonics, Nepal and Tibet. International Federation of Digital Seismograph Networks. Other/Seismic Network. doi:10.7914/SN/YL_2001.

Sheehan, A. F., de la Torre, T. L., Monsalve, G., Abers, G. A., & Hacker, B. A. (2013). Physical state of Himalayan crust and uppermost mantle: Constraints from seismic attenuation and velocity tomography. *J. Geophys. Res. Solid Earth*, *119*, 567–580. doi:10.1002/2013JB010601.

Shi, F., Wang, Y., Yu, T., Zhu, L., Zhang, J., Wen, J., Gasc, J., Incel, S., Schubnel, A., Li, Z., Chen, T., Liu, W., Prakapenka, V., & Jin, Z. (2018). Lower-crustal earthquakes in southern tibet are linked to eclogitization of dry metastable granulite. *Nature Communications*, *9*. doi:10.1038/s41467-018-05964-1.

Silwal, V., & Tape, C. (2016). Seismic moment tensors and estimated uncertainties in southern Alaska. *J. Geophys. Res. Solid Earth*, *121*, 2772–2797. doi:10.1002/2015JB012588.

Swiss Seismological Service (SED) (2013). GANSSER broadband seismic experiment in Bhutan. ETH Zurich. doi:10.12686/sed/networks/xa.

Tape, W., & Tape, C. (2012). A geometric setting for moment tensors. *Geophys. J. Int.*, *190*, 476–498. doi:10.1111/j.1365-246X.2012.05491.x.

Tape, W., & Tape, C. (2013). The classical model for moment tensors. *Geophys. J. Int.*, *195*, 1701–1720. doi:10.1093/gji/ggt302.

Tape, W., & Tape, C. (2015). A uniform parameterization of moment tensors. *Geophys. J. Int.*, *202*, 2074–2081. doi:10.1093/gji/ggv262.

Tape, W., & Tape, C. (2016). A confidence parameter for seismic moment tensors. *Geophys. J. Int.*, *205*, 938–953. doi:10.1093/gji/ggw057.

Tarantola, A. (2005). *Inverse Problem Theory and Methods for Model Parameter Estimation*. Philadelphia, Penn., USA: SIAM.

Wittlinger, G., Farra, V., Hetényi, G., Vergne, J., & Nábělek, J. (2009). Seismic velocities in southern tibet lower crust: a receiver function approach for eclogite detection. *Geophys. J. Int.*, *177*, 1037–104. doi:10.1111/j.1365-246X.2008.04084.x.

Zhao, L.-S., & Helmberger, D. V. (1994). Source estimation from broadband regional seismograms. *Bull. Seismol. Soc. Am.*, *84*, 91–104.

Zhu, L., & Ben-Zion, Y. (2013). Parameterization of general seismic potency and moment tensors for source inversion of seismic waveform data. *Geophys. J. Int.*, *194*, 839–843. doi:10.1093/gji/ggt137.

Zhu, L., & Helmberger, D. (1996). Advancement in source estimation techniques using broadband regional seismograms. *Bull. Seismol. Soc. Am.*, *86*, 1634–1641.

Zhu, L., & Rivera, L. A. (2002). A note on the dynamic and static displacements from a point source in multilayered media. *Geophys. J. Int.*, *148*, 619–627. doi:10.1046/j.1365-246X.2002.01610.x.